

# Numerical Investigation of Three-Dimensional Separation in an Axial Flow Compressor: The Influence of Freestream Turbulence Intensity and Endwall Boundary Layer State

Ashley D. Scillitoe<sup>1</sup>

CFD Laboratory,  
Department of Engineering,  
University of Cambridge,  
Cambridge CB2 1PZ, UK

Paul G. Tucker

CFD Laboratory,  
Department of Engineering,  
University of Cambridge,  
Cambridge CB2 1PZ, UK

Paolo Adami

CFD Methods,  
Rolls-Royce Deutschland,  
Eschenweg 11,  
Blankenfelde-Mahlow 15827, Germany

Regions of three-dimensional separations are an inherent flow feature of the suction surface-endwall corner in axial compressors. These corner separations can cause a significant total pressure loss and reduce the compressor's efficiency. This paper uses wall-resolved LES to investigate the loss sources in a corner separation, and examines the influence of the inflow turbulence on these sources. Different subgrid scale (SGS) models are tested and the choice of model is found to be important. The  $\sigma$  SGS model, which performed well, is then used to perform LES of a compressor endwall flow. The time-averaged data are in good agreement with measurements. The viscous and turbulent dissipation are used to highlight the sources of loss, with the latter being dominant. The key loss sources are seen to be the 2D laminar separation bubble and trailing edge wake, and the 3D flow region near the endwall. Increasing the freestream turbulence (FST) intensity changes the suction surface boundary layer transition mode from separation induced to bypass. However, it does not significantly alter the transition location and therefore the corner separation size. Additionally, the FST does not noticeably interact with the corner separation itself, meaning that in this case the corner separation is relatively insensitive to the FST. The endwall boundary layer state is found to be significant. A laminar endwall boundary layer separates much earlier leading to a larger passage vortex. This significantly alters the endwall flow and loss. Hence, the need for accurate boundary measurements is clear. [DOI: 10.1115/1.4034797]

## Introduction

Over-turning of the endwall boundary layer causes a three-dimensional separation to form in the corner formed by the suction surface and endwall of axial compressors. A number of studies have discussed the importance of these corner separations in both stator and rotor blades [1,2]. They can cause passage blockage and effectively limit the loading and static pressure rise achievable by the compressor. Additionally, they may cause a significant total pressure and a reduction in the compressor's efficiency.

Traditionally, the size of three-dimensional separations has been correlated to global parameters such as inlet and exit flow angles, and pitch to chord ratio. An example of this is the endwall diffusion parameter and corner stall metric proposed by Lei et al. [3]. These are useful in the early design stage, but to maximize the compressor efficiency, it is important to consider the 3D separation in more detail. For example, Goodhand and Miller [4] examined the sensitivity of the 3D separation to small leading edge geometry features, while Gbadebo et al. [5] studied the influence of surface roughness on the 3D separation. Both of these studies conclude that any process leading to premature boundary layer transition on the early suction surface, near the endwalls,

will dramatically increase the size of the 3D separation. This is due to the suction surface boundary layer being excessively thickened.

Premature suction surface boundary layer transition may be caused by leading edge geometry or surface roughness; however, it could also be caused by incoming freestream turbulence (FST). Zaki et al. [6] used direct numerical simulation (DNS) to study the influence of FST intensity on the transitional processes on a compressor blade. They found that the mode and location of the boundary layer transition is very sensitive to the FST intensity. This was at a Reynolds number of  $Re_c = 0.14 \times 10^6$ , and this sensitivity would be expected to decrease at higher Reynolds numbers, with the boundary layers eventually becoming fully turbulent. However, Steinert and Starken [7] showed experimentally that at  $Re_c = 0.84 \times 10^6$  and  $T_i = 2.5\%$ , the suction surface boundary layer stayed laminar to peak suction over a wide range of incidences. At cruise, Reynolds numbers between  $0.4 \times 10^6$  and  $1.6 \times 10^6$  are seen in aero-gas turbine compressors [4]. Therefore, the FST may have an important effect on the 3D corner separation in compressors.

With the above in mind, this paper presents a series of numerical investigations intended to address the following:

- (a) The effect of the FST intensity on the suction surface boundary layer, and therefore the 3D corner separation, is examined. The existence of any direct interaction between the FST and corner separation is also considered.
- (b) Gbadebo [8] found that the 3D separation is also sensitive to the thickness of the incoming endwall boundary layer.

<sup>1</sup>Corresponding author.

Contributed by the International Gas Turbine Institute (IGTI) of ASME for publication in the JOURNAL OF TURBOMACHINERY. Manuscript received July 25, 2016; final manuscript received September 9, 2016; published online October 26, 2016. Editor: Kenneth Hall.

**Table 1 Geometrical and inflow parameters for the two compressor cascades**

	Cascade 1	Cascade 2
Blade profile	NACA-65	CDA
$Re_c$	$1.38 \times 10^5$ (DNS)	$2.30 \times 10^5$
$h/c$	1.36	1.32
$S/c$	0.55	0.926
$t/c$	0.055	0.1
$i$ ( $^\circ$ )	-6.0	0.0
Flow turning (deg)	36.0	33.0
2D Diffusion Factor	0.42	0.49

Taking this further, this paper examines whether the endwall boundary layer state (i.e., laminar versus turbulent) is important.

- (c) Denton [9] investigated the loss sources in the 3D separation region using the entropy generation rate. In a similar manner, this paper uses the viscous and turbulent dissipation to identify the loss sources. In particular, the effect of the inflow conditions on these loss sources will be studied.

Large eddy simulation (LES) will be used for the numerical investigations outlined above. Lardeau et al. [10] found that LES can successfully predict the transitional processes occurring in a compressor flow, at a fraction of the cost of a DNS. However, the subgrid scale (SGS) models used (MTS and dynamic Smagorinsky) require additional filtering, which is problematic for the 3D endwall geometry considered here. To investigate whether such advanced SGS models are necessary, a number of purely local SGS models are first tested on a simpler quasi-2D blade geometry.

## Flow Configurations

The two linear compressor blade cascades detailed in Table 1 are simulated in this paper. Both are representative of highly loaded compressor stator blades found in a modern gas-turbine compressor. Cascade 1 consists of NACA-65 aerofoils and was tested experimentally by Hilgenfeld and Pfitzner [11]. This cascade was also simulated at a lower  $Re_c$  using DNS by Zaki et al. [6] and using LES by Lardeau et al. [10]. Cascade 2 is a linear controlled diffusion aerofoil (CDA) cascade investigated experimentally by Gbadebo et al. [8,12].

The computational grid for cascade 2 is displayed in Fig. 1. A similar H-O-H topology is used for cascade 1. Downstream of the blade, a sponge zone is used to prevent reflections from the outflow boundary. Pitchwise periodicity is enforced with periodic boundaries at midpitch. Some of the cases run are spanwise

**Table 2 The LES cases**

Case	Cascade	Endwall present?	FST Intensity, $T_i$	Endwall BL
1-L-N	1	No	Low (3.25%)	N/A
2-L-N	2	No	Low (1.0%)	N/A
2-L-LBL	2	Yes	Low (1.0%)	LBL
2-L-TBL	2	Yes	Low (1.0%)	TBL
2-H-TBL	2	Yes	High (10.0%)	TBL

periodic (i.e., no endwalls), with periodic boundaries in the spanwise direction. The spanwise extent of these cases is set to 20% span to match the Zaki et al.'s DNS case [6]. The cascade 2 geometry is symmetric about the midspan; however, to prevent contamination of the flow near the midspan, an inviscid wall is placed at 65% span for the cases with an endwall. The endwall is represented by a no-slip wall.

The O-mesh for cascade 1 has dimensions  $690 \times 45 \times 136$  and for cascade 2, it has dimensions  $726 \times 60 \times 557$ . Approximately, 9.3 M grid points are used in the cascade 1 mesh and 69 M for cascade 2. The mesh for cascade 2 is significantly larger due to the larger span, higher  $Re_c$ , and need to resolve the endwall boundary layer. For all the cases,  $\Delta^+ < 50/1/15$  in the tangential/normal/spanwise directions at the wall. These grid resolutions are well within the recommended values for wall-resolved LES given by Piomelli and Chasnov [13].

The LES cases run for this paper are listed in Table 2. Case 1-L-N is a quasi-2D case, with spanwise periodic boundaries. The inflow turbulence intensity ( $T_i$ ) is set at 3.25% to match the DNS of Zaki et al. [6]. This case is used to investigate the performance of a number of subgrid scale models in a transitional compressor flow.

To investigate the effect of inflow conditions on the endwall flow region, three simulations of cascade 2 are run with different inflow conditions. Case 2-L-TBL is intended to match the experiment run by Gbadebo et al. [8,12]. The endwall boundary layer and the FST intensity are measured in the experiment 2 C upstream of the leading edge. To determine the boundary layer parameters at the LES inflow location, the boundary layer from a precursor Reynolds-averaged Navier-Stokes simulation is measured at  $x/C_x = -0.45$ , and the results are presented in Table 3.

The measured shape factor and velocity profile at  $x = -2 C$  suggest that the boundary layer is neither fully laminar nor turbulent, with it perhaps having been partly relaminarized by the upstream contraction in the test rig. Hence, there is a degree of uncertainty here since the RANS simulation assumes a fully turbulent boundary layer at  $x/C = -2$ .

The inflow FST intensity in the cascade 2 experiment is 1.5% [8]. To estimate the FST intensity at the LES inflow ( $x/C_x = -0.45$ ), the following equation from Spalart and Rumsey [14] is used:

$$k = k_{FS} \left[ 1 + (C_{e2} - 1) \left( \frac{\varepsilon}{k} \right)_{FS} \frac{x}{U_1} \right]^{\frac{-1}{C_{e2}-1}} \quad (1)$$

where FS denotes the original inflow conditions at  $x/C = -0.2$  and  $k$  is the freestream turbulent kinetic energy at  $x/C_x = -0.45$ . Approximating  $\varepsilon_{FS} = k_{FS}^{3/2}/L_e$  with  $L_e = 2.2L$ , gives an FST

**Table 3 Endwall boundary layer parameters**

$x =$	$-2.0 C$	$-0.45 C_x$
$\delta_0$	$0.036 C_x$	$0.060 C_x$
$Re_\theta$	440	1350
$Re_{\delta^*}$	770	1850
$H$	1.75	1.37

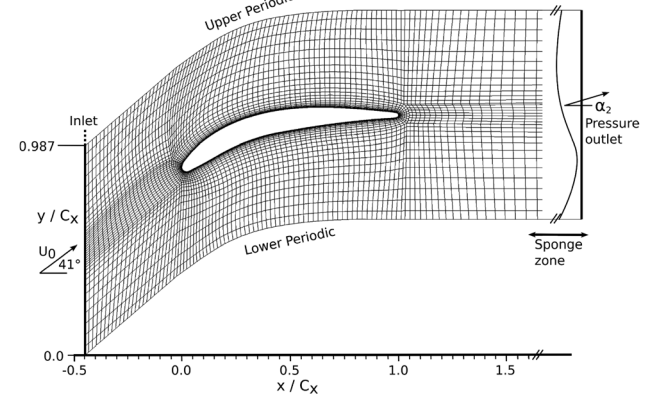


**Fig. 1 Two-dimensional slice of computational grid for cascade 2, showing every fifth grid point**

intensity  $T_i \approx 1.0\%$  at  $x/C_x = -0.45$ . The integral length scale of the freestream turbulence is chosen as  $L = 0.06 C_x$  for all cases, which is the same as that used in the simulations of Zaki et al [6].

## Numerical Method

The code used is the Rolls-Royce CFD code *Hydra* [15]. It is a second-order unstructured, mixed element, compressible finite-volume code. Temporal discretization is performed with a standard five-stage Runge–Kutta algorithm. To improve the code's performance at low Mach numbers, the code has been modified to evaluate the pressure using an artificial compressibility method [16]. This modified code has been successfully used for a number of low pressure turbine LES studies [17,18].

**Subgrid Scale Modeling.** In order to examine the effect of subgrid scale (SGS) modeling on transitional compressor flows, a number of SGS models are investigated in this paper.

The first SGS model used is the Smagorinsky model [19], which defines the SGS viscosity as

$$\mu_{sgs} = \rho \Delta_{sgs}^2 \sqrt{2 \mathbf{S}_{ij} \mathbf{S}_{ij}} \quad (2)$$

where  $\mathbf{S}_{ij}$  is the instantaneous strain rate tensor. The Smagorinsky model is still one of the most widely used SGS models, despite it having some major limitations [20]. For example, incorrect limiting behavior near the wall and the model not vanishing in laminar flow. The model's near-wall behavior is improved here by using wall damping  $\Delta_{sgs} = \min(C_s \Delta_{vol}, \kappa d)$ ; however, this still gives  $\mu_{sgs} = O(d^2)$  instead of the desired  $\mu_{sgs} = O(d^3)$ .

One way to solve the above problems is to modify the Smagorinsky constant  $C_s$  dynamically, as is done in the procedure proposed by Germano et al. [20]. However, this requires additional filtering making it expensive and impractical for LES of complex geometries. As an alternative, Nicoud and Ducros [21] propose the wall-adapting local eddy viscosity (WALE) model

$$\mu_{sgs} = \rho (C_w \Delta_{vol})^2 \frac{\left( \mathbf{S}_{ij}^d \mathbf{S}_{ij}^d \right)^{3/2}}{\left( \mathbf{S}_{ij} \mathbf{S}_{ij} \right)^{5/2} + \left( \mathbf{S}_{ij}^d \mathbf{S}_{ij}^d \right)^{5/4}} \quad (3)$$

The  $\mathbf{S}_{ij}^d \mathbf{S}_{ij}^d$  term is based on both strain and vorticity and is formulated to give zero SGS viscosity in pure shear regions such as a laminar boundary layer.

The final model tested is the  $\sigma$  model also proposed by Nicoud et al. [22], which bases the SGS viscosity on the singular values ( $\sigma_1, \sigma_2, \sigma_3$ ) of the resolved velocity gradient tensor

$$\mu_{sgs} = \rho (C_\sigma \Delta_{vol})^2 \frac{\sigma_3 (\sigma_1 - \sigma_2)(\sigma_2 - \sigma_3)}{\sigma_1} \quad (4)$$

In addition to correctly returning zero SGS viscosity in the case of pure shear, the  $\sigma$  model also correctly gives zero SGS viscosity for solid rotation, plus axisymmetric and isotropic contraction/expansion. Both the WALE and  $\sigma$  models also give  $\mu_{sgs} = O(d^3)$  as desired.

The WALE and  $\sigma$  model constants recommended by Nicoud et al. [21,22] ( $C_w = 0.5$  and  $C_\sigma = 1.35$ ) are used. For isotropic decaying turbulence, these constants give dissipation equal to using the Smagorinsky model with  $C_s \approx 0.165$ ; therefore, this value is chosen for the Smagorinsky model here.

**Time-Dependent Inflow Conditions.** For the endwall test case with an incoming laminar boundary layer (Case 2-L-LBL), an approximate sinusoidal Blasius velocity profile is prescribed with  $\delta_0 = 0.06 C_x$ . For the cases with a turbulent endwall boundary

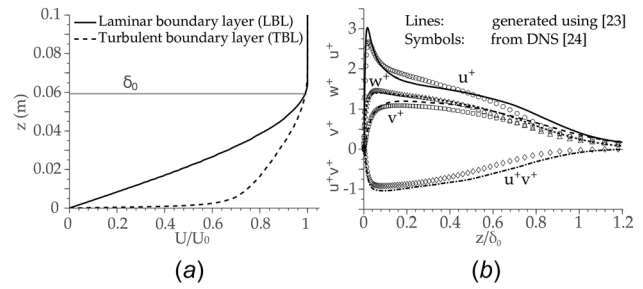


**Fig. 2 Endwall boundary layer profiles at inflow: (a) mean velocity profiles and (b) velocity fluctuations and shear stress profiles (nondimensionalized by  $u_r$ )**

layer (TBL) at the inflow (2-L-TBL and 2-H-TBL), a precursor LES was performed to obtain the time-series data of the incoming TBL. Lund's recycling/rescaling technique [23] is used to generate a streamwise growing TBL, and the time-series data are saved at  $Re_\theta = 1350$ . The generated laminar boundary layer (LBL) and TBL are seen to have the same  $\delta_0$  thickness in Fig. 2(a). The velocity fluctuations and shear stress profiles for the generated TBL also agree well with a DNS of a TBL ( $Re_\theta = 1410$ ) performed by Spalart [24], as shown in Fig. 2(b).

For all the test cases, freestream velocity fluctuations were superimposed onto the mean inflow velocity. These quasi-isotropic perturbations were synthetically generated by a code kindly provided by Dr. Lardeau. The code uses a Fourier-series method [21], and the fluctuations generated satisfy both continuity and the modified von Karman energy spectrum, given by:

$$E(\kappa) = \frac{2}{3} \frac{a(\kappa/\kappa_p)^4}{\left( b + (\kappa/\kappa_p)^2 \right)^{17/6}} \quad (5)$$

where  $a = 1.606$ ,  $b = 1.35$ ,  $\kappa$  is the wave number, and  $\kappa_p$  is the wave number of maximum energy ( $\kappa_p = 1.8/L$ ). For further details, see Refs. [10] and [25].

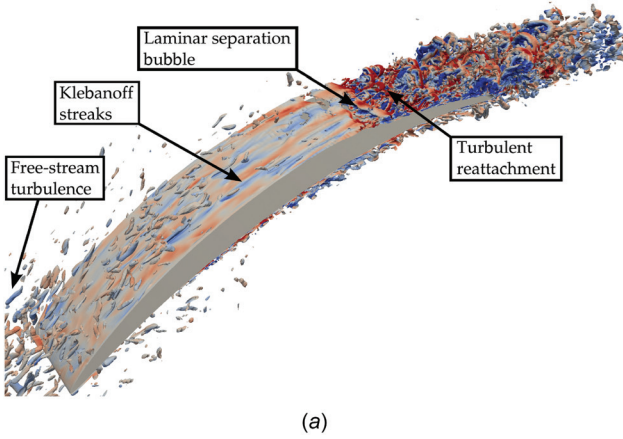
**Simulation Time/Cost.** The time-step is set to give  $CFL_{max} \approx 0.8$ , and a flow-through time ( $T^*$ ) equates to approximately 10,000 time-steps. The simulations were run for  $4T^*$  to clear the initial transients. The quasi-2D cases were then run for  $4T^*$  to collect statistics, while the fully 3D cases had to be run for  $10T^*$  due to the lack of spanwise averaging.

All simulations were run on ARCHER, the UK's National HPC facility. ARCHER is a Cray XC30 MPP supercomputer consisting of 4920 compute nodes, each with two 12-core Intel Ivy Bridge Processors. The quasi-2D cases were run on 128 cores, with each case requiring 12 k CPU hours in total. The fully 3D cases were run on 960 cores, with each case requiring 161 k CPU hours in total.

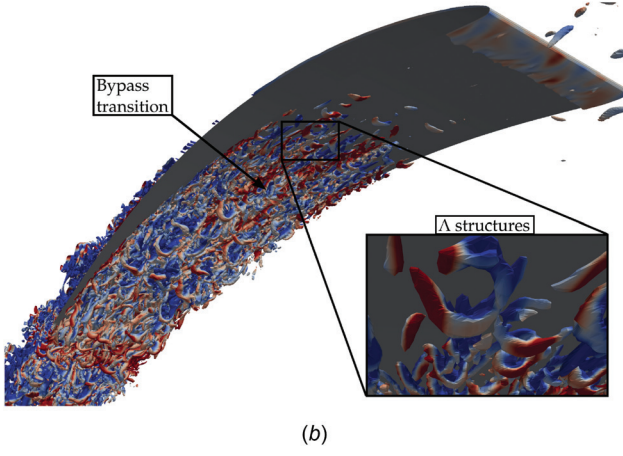
## Cascade 1: Quasi-2D Case

In this section, the LES case 1-L-N is compared to DNS case T1 of Zaki et al. [6]. Figure 3 gives a visual representation of the boundary layer transition processes on the blade surfaces. The Q-criterion, which represents the local balance between shear strain and vorticity magnitude, is used to identify vortices. Qualitatively, the LES agrees well with the DNS.

On the suction surface (Fig. 3(a)), a region of elongated low- and high-speed streaks is observed upstream of transition. The attached laminar boundary layer then separates. In this laminar separation region, or "bubble," spanwise orientated structures associated with Kelvin–Helmholtz (KH) modes are seen. Transition occurs here, and the flow then reattaches to form a turbulent boundary layer.



(a)



(b)

**Fig. 3 Iso-surfaces of positive Q-Criterion colored by streamwise vorticity for case 1-L-N (a) suction surface and (b) pressure surface**

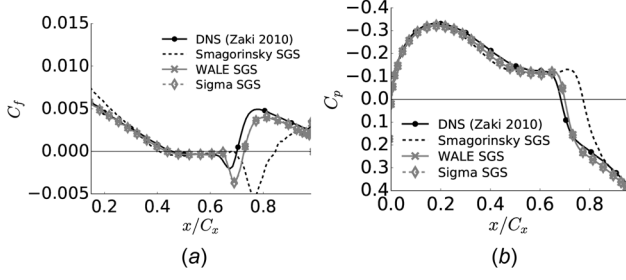


**Fig. 4 Spanwise-averaged  $C_f$  and  $C_p$  distributions on suction surface: (a) friction coefficient and (b) pressure coefficient**

On the pressure surface (Fig. 3(b)), a transition to turbulence occurs much earlier. A “natural” transition involving the amplification of Tollmien-Schlichting (TS) waves is bypassed due to the FST. However,  $\Delta$  structures were observed in the DNS. These are often an indication of natural transition mechanisms [6], implying that the FST intensity may not be high enough for natural transition to be completely bypassed. Such structures are also observed in the LES as highlighted in Fig. 3(b).

The flow on both surfaces is now analyzed in more detail, with particular emphasis on the sensitivity to the SGS model.

**Suction Surface.** Figure 4 shows the suction surface  $C_f$  and  $C_p$  distributions. From the  $C_f$  distributions, the laminar separation bubble onset and reattachment locations, presented in Table 4, are

**Table 4 Separation bubble onset and reattachment locations**

	Onset		Reattachment	
	$x/C_x$	Error (% $C_x$ )	$x/C_x$	Error (% $C_x$ )
DNS [6]	0.447	N/A	0.705	N/A
Smagorinsky	0.418	-2.9	0.853	+14.8
WALE	0.459	+1.2	0.738	+3.3
$\Sigma$	0.459	+1.2	0.738	+3.3

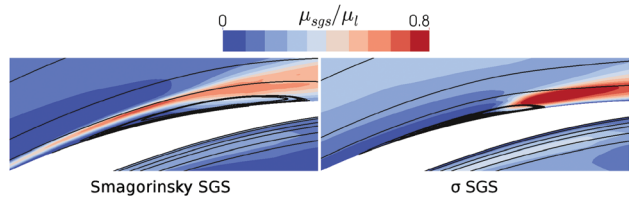


**Fig. 5 Contours of span-averaged SGS viscosity ratio near separation bubble**

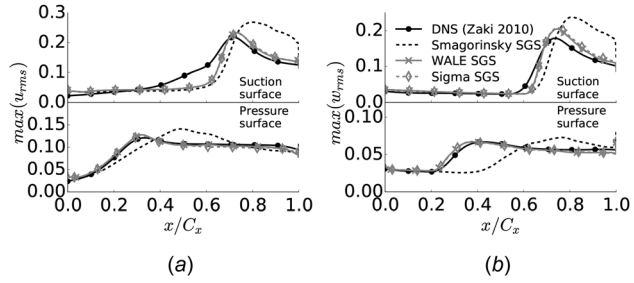


**Fig. 6 Wall normal maximum of streamwise and spanwise velocity fluctuations inside the suction and pressure surface boundary layers: (a) Streamwise,  $u_{rms}$  and (b) spanwise,  $w_{rms}$**

obtained. Compared to the DNS, the Smagorinsky SGS model is seen to predict the onset of separation much too early, leading to an overly large separation bubble. The WALE and  $\sigma$  SGS models do significantly better here, and this is reflected in the  $C_p$  distributions in Fig. 4(b). There is however still a slight overprediction in the bubble length compared to the DNS.

The disagreement between the SGS models arises from the different SGS viscosities they return. Figure 5 shows that the Smagorinsky model incorrectly returns a high SGS viscosity on the edge of the laminar boundary layer upstream of transition. In contrast, since it is pure shear here, the WALE (not shown) and  $\sigma$  models predict a very low level of SGS viscosity.

One may hypothesize that the high SGS viscosity from the Smagorinsky model is damping the development of instabilities in the laminar boundary layer, leading to early separation. However, from Fig. 6, it is apparent that, upstream of transition, the suction surface root mean square (RMS) velocities in all three LES cases agree quite well. It is only after the onset of the separation bubble that the Smagorinsky velocity fluctuations begin to deviate significantly from the DNS. Instead, it appears, from Fig. 7, that the high eddy viscosity in the laminar boundary layer is causing the boundary layer to grow too fast. The thicker suction surface boundary layer in the Smagorinsky simulation, and the adverse pressure gradient, mean that the boundary layer is more susceptible to separation.

The velocity fluctuations from the  $\sigma$  and WALE model simulations mostly agree well with the DNS. The most noticeable difference is that  $u_{rms}$  does not increase between  $0.4 < x/C_x < 0.6$  to the same extent as in the DNS (see Fig. 6(a)). Zaki et al. [6] note that

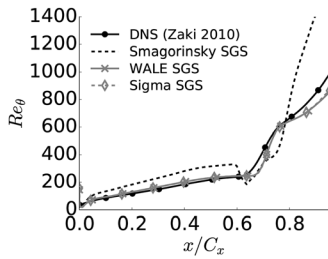


Fig. 7 Span-averaged  $Re_\theta$  along suction surface

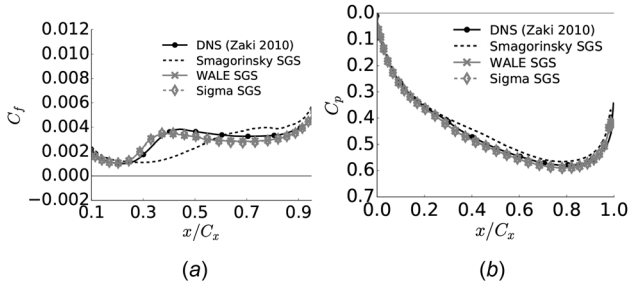


Fig. 8 Pressure surface  $C_f$  and  $C_p$  distributions: (a) Friction coefficient and (b) pressure coefficient

$u_{rms}$  dominating over  $v_{rms}$  and  $w_{rms}$  here hints at the presence of Klebanoff streaks [6]. Thus, it appears that the magnitude of these Klebanoff modes is underpredicted in the present LES cases, which may help explain the slight overprediction in bubble length. In the LES computations of Lardeau et al. [10], the opposite is found, with the magnitude of the Klebanoff modes being significantly overpredicted. Future work will investigate the cause of this discrepancy.

**Pressure Surface.** It is obvious from the pressure surface  $C_f$  distributions in Fig. 8(a) that the Smagorinsky model leads to a significant delay in the pressure surface transition location. With the separation-induced transition (on the suction surface), the high SGS viscosity from the Smagorinsky model causes excessive boundary layer growth but does not damp  $u_{rms}$  and  $w_{rms}$ . However, examining the velocity fluctuations in Fig. 6, it would appear that  $u_{rms}$  and  $w_{rms}$  in the pressure surface transition region are being damped by the Smagorinsky model. The high SGS viscosity appears to damp the growth of instabilities associated with natural and bypass transition, leading to delayed transition.

The  $C_f$  and  $C_p$  distributions in Fig. 8 and the velocity fluctuations in Fig. 6 show that the WALE and  $\sigma$  SGS models agree closely with the pressure surface DNS results.

## Cascade 2: 3D Case

In the previous section (Cascade 1: Quasi-2D Case), the  $\sigma$  SGS model was shown to predict the transitional processes seen on a compressor blade far better than the Smagorinsky model. For this reason, the  $\sigma$  model is used for all the simulations of Cascade 2 discussed in this section.

**Validation Against Experiment.** Case 2-L-TBL is intended to be representative of the experiment run by Gbadebo et al. [8,12]. Figure 9 compares the surface limiting streamlines from the time-averaged LES and the experimental oilflow. Qualitatively, case 2-L-TBL agrees well with the experiment; a laminar separation bubble is seen on the suction surface in both, the origin of suction surface corner separation is closely predicted, and the corner separation line extends away from the endwall at a similar angle in both. Below the separation line, the flow topology also appears to be closely matched.

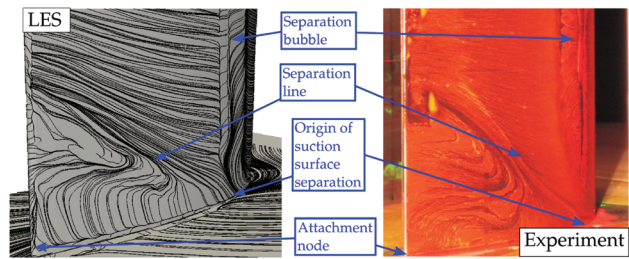
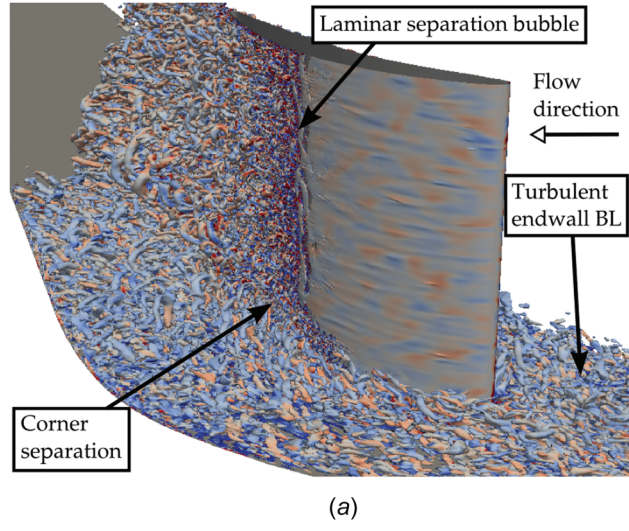
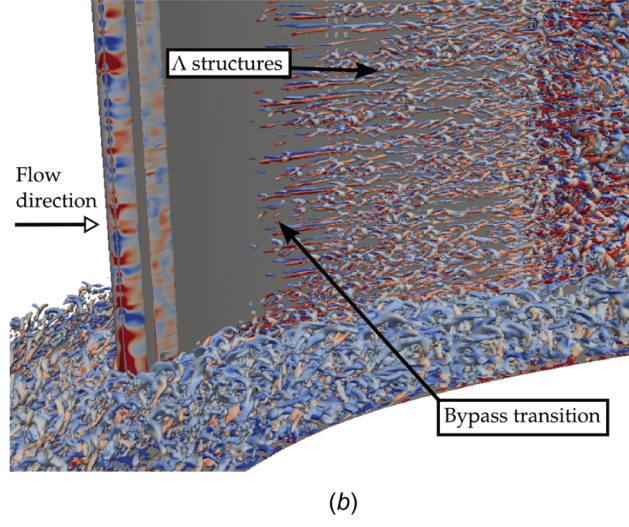


Fig. 9 LES surface streamlines and experimental oilflow



(a)



(b)

Fig. 10 Instantaneous iso-surfaces of positive Q-criterion colored by streamwise vorticity for case 2-L-TBL: (a) suction surface and (b) pressure surface

The transitional processes occurring in case 2-L-TBL are visualized using iso-surfaces of Q-criterion in Fig. 10. The processes observed are very similar to those seen on Cascade 1 previously, with separation-induced transition on the suction surface and bypass transition on the pressure surface. Also observable is the turbulent endwall boundary layer, and the highly turbulent region in the endwall suction-surface corner.

The  $C_p$  distributions for case 2-L-TBL, seen in Fig. 11, generally agree well with the experiment. However, there is some deviation from the experimental  $C_p$  distribution close to the

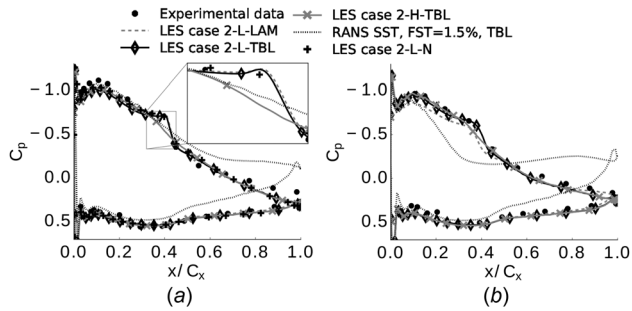


Fig. 11  $C_p$  distributions near endwall and midspan

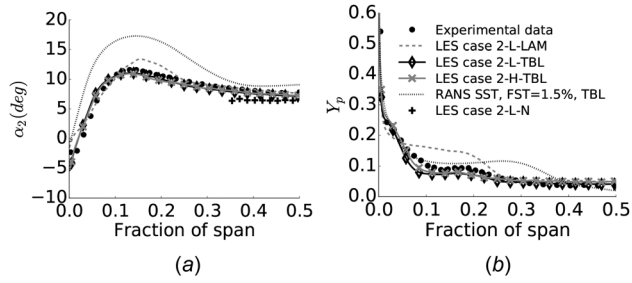


Fig. 12 Pitchwise mass-averaged exit angle and loss coefficient versus span at  $x/C_x = 1.5$ : (a) exit angle and (b) loss coefficient streamwise,  $u_{rms}^2$

trailing edge near the midspan (Fig. 11(b)). This is not due to contamination from the upper inviscid boundary since the spanwise periodic simulation (case 2-L-N) shows the same deviation.

The pitch-wise mass-averaged exit angle and loss coefficient are plotted against span in Figs. 12(a) and 12(b). The downstream exit angle prediction from case 2-L-TBL is in good agreement with the experiment.

The downstream loss prediction also agrees well, with only a slight deficit in the predicted loss between 5% and 25% span. Despite a few small differences between case 2-L-TBL and the experiment, as expected, it still gives a much better prediction of the flow compared to a blind RANS computation, as is seen in Figs. 11 and 12.

**Effect of Endwall Boundary Layer State.** The effect of the endwall boundary state (case 2-L-TBL versus case 2-L-LBL) is visualized in Fig. 13. The surface limiting streamlines suggest endwall boundary layer state does not significantly affect the flow topology on the blade, especially closer to the midspan. The transition location, observable from the peak in  $u_{rms}$ , is also not noticeably altered.

The key difference is that the laminar endwall boundary layer cannot resist the adverse pressure gradient and so it separates much earlier, observable from the more upstream endwall saddle point in Fig. 13(b) compared to Fig. 13(a). This leads to a much larger pressure leg of the horseshoe vortex, which migrates down from the blade above, interacts with the corner separation, and results in a large passage vortex, as seen in Fig. 13(b).

Comparing cases 2-L-TBL and 2-L-LBL in Figs. 11(a) and 12 shows that the larger passage vortex has a significant impact on the pressure distribution, exit flow angle, and loss coefficient near the endwall. However, Figs. 14 and 15 confirm that the state of the endwall BL has not significantly altered the flow at midspan.

**Effect of Freestream Turbulence.** Comparing cases 2-L-TBL and 2-H-TBL in Figs. 11 and 12 suggests that increasing the FST

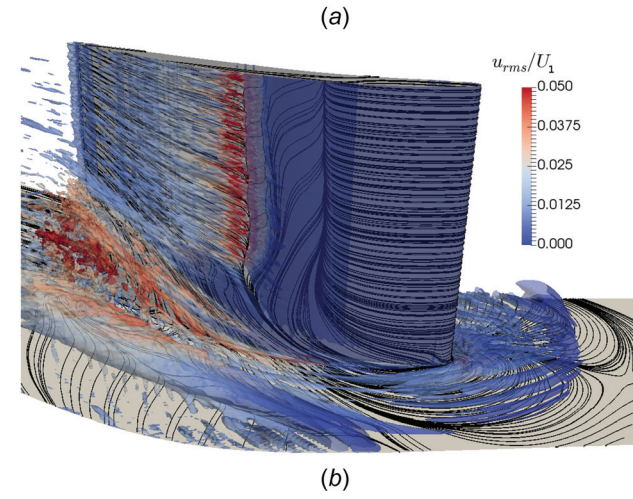
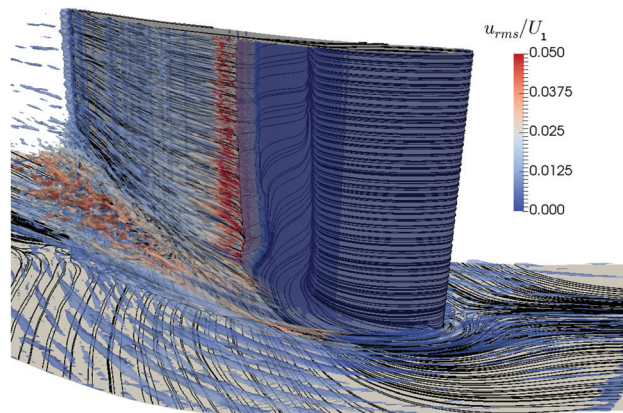


Fig. 13 Time-averaged iso-surfaces of vorticity magnitude colored by  $u_{rms}$ : (a) Case 2-L-TBL and (b) Case 2-L-LBL

intensity by an order of magnitude has had little effect on the flow near the endwall. This is surprising, since Goodhand and Miller [4] show that if the transition point moves upstream the thickened suction surface boundary layer will lead to a larger endwall separation. Figure 14(a) shows that despite the higher FST intensity changing the suction surface transition mode from separation induced to bypass, the transition location is not altered significantly. Thus, it seems that if the transition location is not altered, the FST has little influence on the endwall separation.

The velocity fluctuations plotted in Fig. 15 confirm that the transition location on the suction surface is similar for both cases. In case 2-H-TBL  $u_{rms}$  dominates over  $v_{rms}$  and  $w_{rms}$  more than in case 2-L-TBL, suggesting the energy carried by Klebanoff modes is higher here. This is consistent with the findings of Zaki et al. [6], where it was found that the energy carried by the Klebanoff modes increases with FST intensity, leading to a faster breakdown of the KH structures and a reduction in the separation bubble length. In case 2-H-TBL, the FST intensity is high enough to completely prevent the boundary layer separating.

Figures 14(b) and 15 show the bypass transition on the pressure surface occurs noticeably earlier with the higher freestream turbulence. However, the pressure surface-endwall corner effects are relatively small so the pressure surface boundary layer is less important.

**Sources of Loss.** The state of the suction surface boundary layer and the freestream turbulence both influence the loss in the passage. To determine the sources of loss and examine the effect of the inflow conditions further, the mean flow energy equation is used

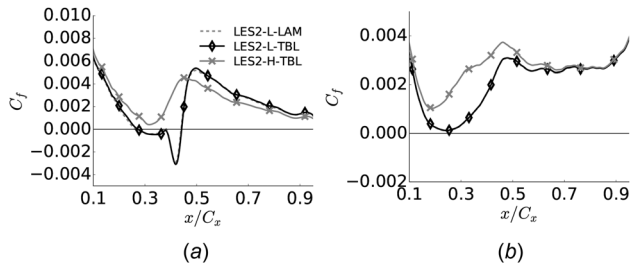


Fig. 14  $C_f$  coefficient at midspan: (a) suction surface and (b) pressure surface

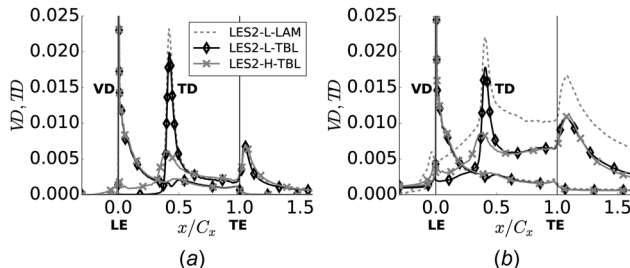


Fig. 16 Area-averaged (in  $y$ - $z$  plane) viscous and turbulent dissipation through blade passage: (a) 35–50% span and (b) 0–35% span

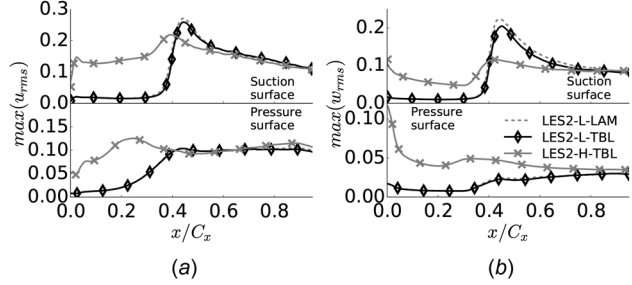


Fig. 15 Wall normal maximums of streamwise and spanwise velocity fluctuations in the blade passage at midspan: (a) streamwise,  $u_{rms}$  and (b) spanwise,  $w_{rms}$

$$\frac{\partial E}{\partial t} + \bar{u}_j \frac{\partial E}{\partial x_j} = \underbrace{\frac{\partial}{\partial x_j} \left( -\bar{u}_j \frac{\bar{p}}{\rho} + 2\nu \bar{u}_j \bar{s}_{ij} - \bar{u}'_i \bar{u}'_j \bar{u}_i \right)}_{\text{Transport}} - \underbrace{2\nu \bar{s}_{ij} \bar{s}_{ij}}_{\text{Viscous dissipation -VD}} + \underbrace{\bar{u}'_i \bar{u}'_j \bar{s}_{ij}}_{\text{Turbulent dissipation -TD}} \quad (6)$$

In Eq. (6), the viscous and turbulent dissipation terms are the only sink (or source) terms. The viscous dissipation represents the dissipation of mean-flow energy by the velocity gradients, and is always negative (i.e.,  $VD > 0$ ). The turbulent dissipation represents the energy transfer from the mean flow into turbulent fluctuations. It is usually negative (i.e.,  $TD > 0$ ), meaning energy is being transferred from the mean flow. However, on some occasions, it can be positive (i.e.,  $TD < 0$ ) implying the presence of turbulent energy backscatter. In cases 2-L-LBL and 2-L-TBL, a negative value of turbulent dissipation (TD) is observed in the separation bubble region. This is in agreement with the work of Germano et al. [20]. They found that during the early nonlinear stages of transition, energy is transferred from smaller to larger scales, even in the mean. However, in the present investigation, no negative TD values are observed in the endwall separation region, suggesting there is no backscatter here (at least within the scales resolved).

Denton and Pullan [26], and Zlatinov et al. [27], use the entropy generation rate to examine the loss sources in a turbine cascade. In a similar way, the TD and viscous dissipation (VD) terms will be used here to examine the loss sources and their sensitivity to the inflow conditions. The flow here is isentropic; therefore, the thermal dissipation does not need to be considered. To differentiate the loss sources caused by the endwall flow, the domain is split into two sections: a lower section (0–35% span) where endwall effects mean the flow is highly three-dimensional, and an upper section (35–50% span) where the flow is largely two-dimensional.

The VD and TD terms are then area averaged (in the pitchwise and spanwise directions) and plotted against axial distance.

In the upper section (Fig. 16(a)), there are three distinct peaks, which identify the high loss generation areas. At the leading edge ( $x/C_x \approx 0.0$ ), VD is high due to the high strain rates near the leading edge. In the vicinity of the 2D separation bubble ( $x/C_x \approx 0.4$ ), TD is high due to the high level of turbulence generated in the free shear layer at the edge of the bubble, which was observed in Fig. 15. Since in case 2-H-TBL, the separation bubble is suppressed, the peak in TD here is lower than for case 2-L-TBL. However, this lower level of TD is offset by the higher FST intensity in the passage and the earlier pressure surface transition. Comparing cases 2-L-TBL and 2-L-LBL suggests that the state of the endwall BL has little effect here. Downstream of the trailing edge ( $x/C_x \approx 1.1$ ) TD is high due to the turbulence generated in the free shear layer at the edges of the trailing edge wake. The inflow conditions appear to have little effect here.

In the lower section close to the endwall (Fig. 16(b)), the three distinct peaks are still present. However, now there is also an area of high turbulent dissipation downstream ( $x/C_x > 0.5$ ) caused by the three-dimensional flow near the endwall. The FST intensity has little influence on the loss in this region, further supporting the conclusion that the 3D endwall flow is insensitive to the FST intensity.

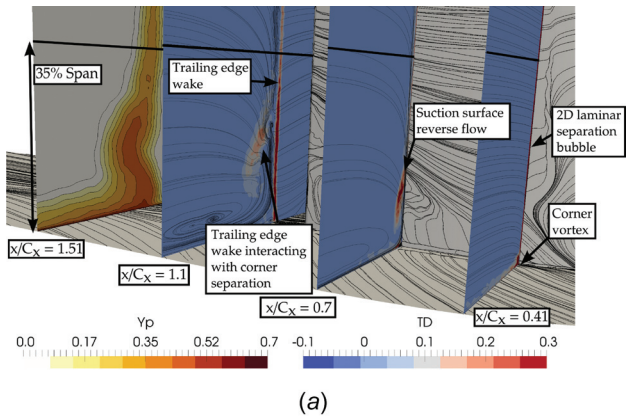
The laminar endwall boundary layer case (2-L-LBL) shows significantly higher turbulent dissipation in the 3D separation region near the endwall ( $x/C_x > 0.5$  in Fig. 16(b)). To elucidate the cause of this, contours of turbulent dissipation at three locations ( $x/C_x = 0.41, 0.7, 1.1$ ) are presented in Fig. 17.

In case 2-L-TBL (Fig. 17(a)), the TD is high in the 3D separation region where there is reverse flow on the suction surface (seen at  $x/C_x = 0.7$ ), and this 3D separation region persists downstream at  $x/C_x = 1.1$ . In case 2-L-LBL (Fig. 17(b)), there is also high TD in the shear layer between the passage vortex and the freestream, and the TD is especially high where the passage vortex interacts with the corner separation close to the suction surface. This high TD causes significantly higher loss, which is observable when comparing the pressure loss coefficient ( $Y_p$ ) contours downstream of the blade in Figs. 17(a) and 17(b).

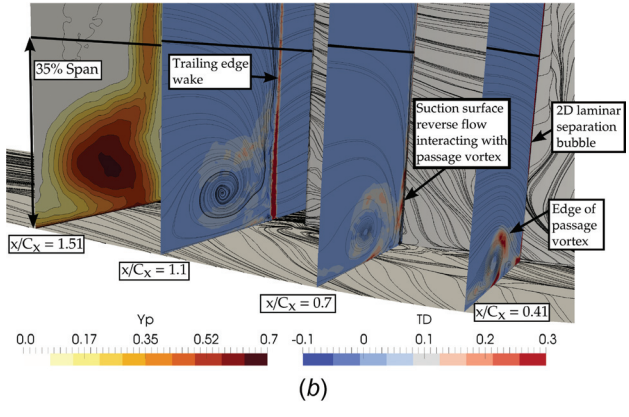
The overall effect of the VD and TD on the loss can be seen by plotting the cumulative integral of the sum of these terms with respect to the axial direction:

$$\phi_{tot}(X) = \int_{x=-0.45C_x}^{x=X} (TD(x) + VD(x)) dx \quad (7)$$

where  $\phi_{tot}(X)$  is the total area-averaged dissipation (VD + TD) so far (i.e., between  $-0.45 C_x < x < X$ ). This is plotted against  $x$  in Fig. 18. Near the midspan (Fig. 18(a)), the high FST intensity in case 2-H-TBL causes a higher  $\phi_{tot}$  early on due to the early pressure surface transition and higher FST intensity in the passage.



(a)



(b)

**Fig. 17** Contours of turbulent dissipation and loss coefficient near endwall: (a) Case 2-L-TBL And (b) Case 2-L-LBL

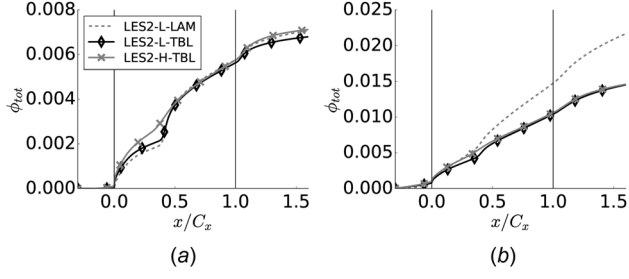


**Fig. 18** Cumulative integral of area-averaged viscous and turbulent dissipation through blade passage: (a) 35–50% span and (b) 0–35% span

However,  $\phi_{tot}$  in the other two cases rapidly increases to rejoin case 2-H-TBL due to the high TD in the separation bubble at  $x/C_x \approx 0.4$ . By the outflow plane at  $x/C_x = 1.52$ , the total dissipation in the upper section is very similar for all three cases, with case 2-L-TBL having a slightly lower total. These findings correlated well with the loss coefficient plot in Fig. 12(b) where the loss at midspan is slightly lower for case 2-L-TBL.

Near the endwall (Fig. 18(b)) where 3D flow effects are significant, the FST has little effect, with the  $\phi_{tot}$  lines for both FST cases following closely. Conversely,  $\phi_{tot}$  increases more rapidly in the LBL case downstream of the separation bubble ( $x/C_x > 0.5$ ) due to the effects of the passage vortex discussed previously. Again, these findings correlate well with the loss coefficient distribution in Fig. 12(b). Near the endwall, the loss in the high and low FST intensity cases is very similar, whereas the loss in the LBL case is much higher here.

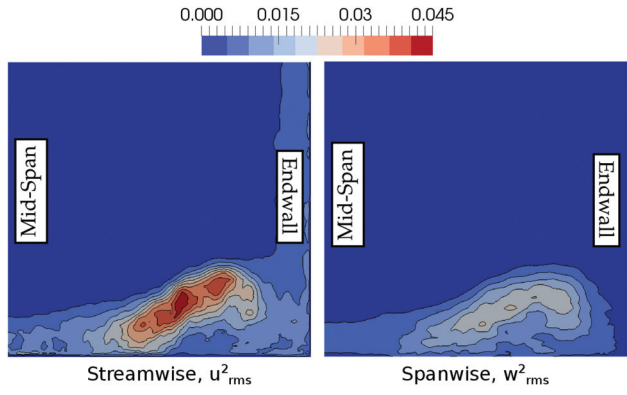


**Fig. 19** Contours of velocity fluctuations at trailing edge, for LES case 2-L-TBL

**Turbulence Characteristics.** Figure 19 shows contours of the streamwise and spanwise RMS velocity at the trailing edge. Examining the separate velocity components shows that the turbulence is anisotropic in the corner separation region. The streamwise fluctuations dominate over the pitch-wise (not shown) and spanwise fluctuations. This has consequences for RANS modeling of such flows, since many RANS models do not correctly account for anisotropy of turbulence.

The velocity fluctuations shown in Fig. 19 correspond to a local turbulence intensity of up to 34%. This high turbulence intensity suggests a possible contribution of endwall separation to broadband noise. Moreover, the significant difference in turbulence intensity between the endwall separation and the FST may help explain why the endwall separation has been found to be relatively insensitive to the FST intensity.

## Conclusions

The following conclusions are drawn from this study:

- (1) The Smagorinsky subgrid scale model is unsuitable for the transitional compressor flows studied. It causes excessive thickening of the suction surface boundary layer, leading to premature separation, and an overprediction of the bubble length. On the pressure surface, it significantly delays the bypass transition. In comparison, the ability of the  $\sigma$  and WALE models to limit the SGS viscosity in the laminar boundary layer means they are more suitable to such flows. These purely local SGS models appear to be able to compete with the dynamic SGS models used by Lardeau et al. [10] for the same case. The ability to use local SGS models will simplify the application of LES to more complex compressor geometries.
- (2) The state of the endwall boundary layer is critical. A laminar endwall boundary layer cannot withstand the adverse pressure gradient near the leading edge and so separates earlier. The larger passage vortex leads to under-turning of the flow and increased loss. In many blade cascade experiments, the endwall boundary layers are partly relaminarized by an upstream contraction. This highlights the need for the endwall boundary layer velocity and stress profiles to be accurately recorded in cascade experiments.
- (3) Increasing the FST intensity caused the suction surface transition mode to change from separation induced to bypass transition. However, this had little effect on the corner separation since the transition location, and therefore the boundary layer thickness, was unaffected. Additionally, the FST was not found to directly influence the corner separation, perhaps due to the much higher turbulence intensity observed in the corner separation region.

- (4) Near the midspan, the viscous dissipation near the leading edge and turbulent dissipation at the 2D separation bubble are the main loss sources. A high FST intensity suppresses the separation bubble, but causes higher loss overall due to the earlier pressure surface transition and higher turbulent dissipation in the freestream. In the 3D flow region near the endwall, the turbulent dissipation dominates. The FST intensity has little effect here. The state of the endwall boundary layer and the size of the passage vortex it results in are more important.

## Acknowledgment

This work was supported by the EPSRC through an iCASE award sponsored by Rolls-Royce plc. Rolls-Royce plc are gratefully acknowledged for allowing the use and modification of their CFD solver HYDRA. The work used the ARCHER UK National Supercomputing Service<sup>2</sup> under EPSRC Grant No. EP/L000261/1, and thanks go to both for their support. Finally, the authors would like to thank Dr. Naqavi, Dr. Watson, and Mr. Cui for their invaluable inputs, Dr. Zaki for providing the geometry for cascade 1, and Dr. Lardeau for providing the inflow turbulence code.

## Nomenclature

- $C$  = blade chord
- $C_f$  = skin friction coefficient,  $\mu_l(\tau_w)/((1/2)\rho U_1^2)$
- $C_p$  = static pressure coefficient,  $(p - p_1)/((1/2)\rho U_1^2)$
- $C_x$  = blade axial chord
- $d$  = wall distance
- $h$  = blade height/span
- $H$  = boundary layer shape factor,  $\delta^*/\theta$
- $i$  = incidence angle
- $k$  = turbulent kinetic energy
- $L$  = integral length scale of turbulence
- $L_e$  = dissipation length scale of turbulence
- $Q$  = Q-criterion,  $((1/2)(|\Omega|^2 - |S|^2))$
- $Re$  = Reynolds number
- $S$  = blade pitch
- $S/\Omega$  = magnitude of strain rate/vorticity tensor,  $\sqrt{2S_{ij}S_{ij}}, \sqrt{2\Omega_{ij}\Omega_{ij}}$
- $S_{ij}/\Omega_{ij}$  = strain rate/Vorticity tensors
- $t$  = blade thickness
- $T_i$  = freestream turbulence intensity
- $T^*$  = flow through time
- $u_\tau$  = friction velocity,  $\sqrt{\tau_w/\rho}$
- $U_1$  = inflow bulk velocity
- $U'_RMS$  = RMS mean velocity,  $\sqrt{1/2(u_{rms}^2 + v_{rms}^2 + w_{rms}^2)}$
- $u_{rms}, v_{rms}, w_{rms}$  = streamwise, wall-normal and spanwise RMS velocities
- $x, y, z$  = axial, pitchwise, spanwise co-ordinates
- $Y_p$  = total pressure loss coefficient,  $(p_0 - p_1)/((1/2)\rho U_1^2)$
- $\alpha_2$  = exit flow angle
- $\delta_0$  = boundary layer thickness based on 0.99  $U_1$
- $\delta^*$  = boundary layer displacement thickness
- $\Delta^+$  = nondimensional grid spacing at wall,  $\Delta\sqrt{\tau_w/\rho}/\nu$
- $\Delta_{vol}$  = cell volume filter,  $\sqrt[3]{\Delta x \Delta y \Delta z}$
- $\Delta_{SGS}$  = subgrid scale model filter
- $\varepsilon$  = turbulent dissipation
- $\theta$  = boundary layer momentum thickness
- $\mu_{sgs}$  = subgrid scale viscosity
- $\mu_l/\mu_t$  = laminar/turbulent viscosity

<sup>2</sup><http://www.archer.ac.uk>

$\sigma_{1/2/3}$  = singular values of the resolved velocity gradient tensor

## Subscripts

- FS = freestream quantity
- 1 = inflow quantity
- 2 = exit quantity

## Abbreviations

- CDA = controlled diffusion aerofoil
- FST = freestream turbulence
- KH = Kelvin-Helmholtz
- LBL = laminar boundary layer
- MTS = mixed time-scale
- RMS = root mean square
- SGS = subgrid scale
- TBL = turbulent boundary layer
- TD = turbulent dissipation
- TS = Tollmien-Schlichting
- VD = viscous dissipation

## References

- [1] Dong, Y., Gallimore, S. J., and Hodson, H. P., 1987, "Three-Dimensional Flows and Loss Reduction in Axial Compressors," *ASME J. Turbomach.*, **109**(3), pp. 354–361.
- [2] Friedrichs, J., Baumgarten, S., Kosyna, G., and Stark, U., 2001, "Effect of Stator Design on Stator Boundary Layer Flow in a Highly Loaded Single-Stage Axial-Flow Low-Speed Compressor," *ASME J. Turbomach.*, **123**(3), pp. 483–489.
- [3] Lei, V. M., Spakovszky, Z. S., and Greitzer, E. M., 2008, "A Criterion for Axial Compressor Hub-Corner Stall," *ASME J. Turbomach.*, **130**(3), p. 031006.
- [4] Goodhand, M. N., and Miller, R. J., 2012, "The Impact of Real Geometries on Three-Dimensional Separations in Compressors," *ASME J. Turbomach.*, **134**(2), p. 021007.
- [5] Gbadebo, S. A., Hynes, T. P., and Cumpsty, N. A., 2004, "Influence of Surface Roughness on Three-Dimensional Separation in Axial Compressors," *ASME J. Turbomach.*, **126**(4), pp. 455–463.
- [6] Zaki, T. A., Wissink, J. G., Rodi, W., and Durbin, P. A., 2010, "Direct Numerical Simulations of Transition in a Compressor Cascade: The Influence of Free-Stream Turbulence," *J. Fluid Mech.*, **665**, pp. 57–98.
- [7] Steinert, W., and Starken, H., 1996, "Off-Design Transition and Separation Behavior of a CDA Cascade," *ASME J. Turbomach.*, **118**(2), pp. 204–210.
- [8] Gbadebo, S. A., 2003, "Three-Dimensional Separations in Compressors," *Ph.D thesis*, University of Cambridge, Cambridge, UK.
- [9] Denton, J. D., 1993, "The 1993 IGTI Scholar Lecture: Loss Mechanisms in Turbomachines," *ASME J. Turbomach.*, **115**(4), p. 621.
- [10] Lardeau, S., Leschziner, M., and Zaki, T., 2011, "Large Eddy Simulation of Transitional Separated Flow Over a Flat Plate and a Compressor Blade," *Flow, Turbul. Combust.*, **88**(1–2), pp. 19–44.
- [11] Hilgenfeld, L., and Pfitzner, M., 2004, "Unsteady Boundary Layer Development Due to Wake Passing Effects on a Highly Loaded Linear Compressor Cascade," *ASME J. Turbomach.*, **126**(4), pp. 493–500.
- [12] Gbadebo, S. A., Cumpsty, N. A., and Hynes, T. P., 2005, "Three-Dimensional Separations in Axial Compressors," *ASME J. Turbomach.*, **127**(2), pp. 331–339.
- [13] Piomelli, U., and Chasnow, J. R., 1996, *Large-Eddy Simulations: Theory and Applications, Turbulence and Transition Modelling*, D. Henningsson, M. Hallbäck, H. Alfredsson, and A. Johansson, eds., Kluwer Academic Publishers, Dordrecht, The Netherlands, pp. 269–336.
- [14] Spalart, P. R., and Rumsey, C. L., 2007, "Effective Inflow Conditions for Turbulence Models in Aerodynamic Calculations," *AIAA J.*, **45**(10), pp. 1–14.
- [15] Crompton, P. I., Moinier, P., and Giles, M. B., 1997, "An Unstructured Algorithm for High Reynolds Number Flows on Highly Stretched Grids," Tenth International Conference on Numerical Methods for Laminar and Turbulent Flow, pp. 561–572.
- [16] Rogers, S. E., Kwak, D., and Kiris, C., 1991, "Steady and Unsteady Solutions of the Incompressible Navier-Stokes Equations," *AIAA J.*, **29**(4), pp. 603–610.
- [17] Cui, J., Nagabhushana Rao, V., and Tucker, P., 2015, "Numerical Investigation of Contrasting Flow Physics in Different Zones of a High-Lift Low-Pressure Turbine Blade," *ASME J. Turbomach.*, **138**(1), p. 011003.
- [18] Cui, J., Nagabhushana Rao, V., and Tucker, P. G., 2015, "Numerical Investigation of Secondary Flows in a High-Lift Low Pressure Turbine," 8th International Symposium Turbulence Heat and Mass Transfer, pp. 1–9.
- [19] Smagorinsky, J., 1963, "General Circulation Experiments With the Primitive Equations," *Mon. Weather Rev.*, **91**(3), mar, pp. 99–164.
- [20] Germano, M., Piomelli, U., Moin, P., and Cabot, W. H., 1991, "A Dynamic Subgrid-Scale Eddy Viscosity Model," *Phys. Fluids A Fluid Dyn.*, **3**(7), p. 1760.
- [21] Nicoud, F., and Ducros, F., 1999, "Subgrid-Scale Stress Modelling Based on the Square of the Velocity Gradient Tensor," *Flow, Turbul. Combust.*, **62**(3), pp. 183–200.

- [22] Nicoud, F., Toda, H. B., Cabrit, O., Bose, S., and Lee, J., 2011, "Using Singular Values to Build a Subgrid-Scale Model for Large Eddy Simulations," *Phys. Fluids*, **23**(8), pp. 1–35.
- [23] Lund, T. S., Wu, X., and Squires, K. D., 1998, "Generation of Turbulent Inflow Data for Spatially-Developing Boundary Layer Simulations," *J. Comput. Phys.*, **140**(2), pp. 233–258.
- [24] Spalart, P. R., 1988, "Direct Simulation of a Turbulent Boundary Layer up to  $R\theta = 1410$ ," *J. Fluid Mech.*, **187**, pp. 61–98.
- [25] Rogallo, R. S., 1981, "Numerical Experiments in Homogeneous Turbulence," *NASA Ames Research Center*, Moffett Field, CA, Technical Report No. NASA-TM- 81315.
- [26] Denton, J., and Pullan, G., 2012, "A Numerical Investigation Into the Sources of Endwall Loss in Axial Flow Turbines," *ASME Paper No. GT2012-69173*.
- [27] Zlatinov, M. B., Sooi Tan, C., Montgomery, M., Islam, T., and Harris, M., 2012, "Turbine Hub and Shroud Sealing Flow Loss Mechanisms," *ASME J. Turbomach.*, **134**(6), p. 061027.